

# Molecular Origins of the Mechanical Behavior of Hybrid Glasses

By Mark S. Oliver, Geraud Dubois,\* Mark Sherwood, David M. Gage, and Reinhold H. Dauskardt\*

Hybrid organic-inorganic glasses exhibit unique electro-optical properties along with excellent thermal stability. Their inherently mechanically fragile nature, however, which derives from the oxide component of the hybrid glass network together with the presence of terminal groups that reduce network connectivity, remains a fundamental challenge for their integration in nanoscience and energy technologies. We report on a combined synthesis and computational strategy to elucidate the effect of molecular structure on mechanical properties of hybrid glass films. We first demonstrate the importance of rigidity percolation to elastic behavior. Secondly, using a novel application of graph theory, we reveal the complex 3-D fracture path at the molecular scale and show that fracture energy in brittle hybrid glasses is fundamentally governed by the bond percolation properties of the network. The computational tools and scaling laws presented provide a robust predictive capability for guiding precursor selection and molecular network design of advanced hybrid organic-inorganic materials.

## 1. Introduction

Hybrid organosilicate glass films processed from small organosilane precursors exhibit unique electro-optical properties while maintaining excellent thermal stability. They can be inexpensively processed using sol-gel or chemical vapor deposition and have application in emerging nanoscience and energy technologies.<sup>[1]</sup> A fundamental challenge for their integration and application, however, remains their inherently mechanically fragile nature that derives from the oxide component of the hybrid glass network and the presence of terminal hydroxyl and organic groups that reduce network connectivity.

Remarkably little fundamental understanding exists of how hybrid glass structure governs even basic mechanical properties like elastic stiffness and cohesive fracture energy, limiting

the design of hybrid molecular networks with improved mechanical properties. We describe molecular modeling strategies that are able to quantitatively predict the effects of hybrid molecular network parameters such as molecular type and condensation degree on elastic and fracture properties. With these models, along with experimental characterization of synthesized glasses, we reveal the fundamental connections between the percolation properties of the glass network and glass mechanical behavior. These findings provide a simple mathematical framework for predicting the mechanical behavior of complex network glasses.

To accurately model hybrid glasses, we first generate large, distortion-free networks using molecular dynamics-based simulated annealing.<sup>[2]</sup> Unlike existing methods for generating model hybrid glasses,<sup>[3–5]</sup> ours does not define the network topology prior to structural relaxation. Another advanced feature of our approach is the ability to generate hybrid glasses with well-controlled network connectivity. This enables systematic variation of the network connectivity and calibration with experimental <sup>29</sup>Si NMR measurements of condensation degree. Elastic properties were predicted with molecular dynamics simulations. To model fracture, we have developed a model using the minimum-cut principle of graph theory to predict the complex three-dimensional cohesive fracture path through hybrid glasses at the atomic scale and provide both the number and types of bonds broken.

The specific glasses investigated were ethane-bridged oxycarbosilane (Et-OCS) and methylated ethane-bridged oxycarbosilane (Et-OCS(Me)) (see **Figure 1**). These represent the state-of-the-art molecular-reinforced hybrid glass films. Recently, it has been demonstrated that the incorporation of alkane bridges in hybrid glasses results in materials with mechanical properties considerably better than glasses containing univalent carbon groups.<sup>[6–9]</sup> When organics are incorporated into hybrid glass networks in the form of univalent carbon groups, the molecular connectivity is disrupted and the mechanical properties are significantly degraded.<sup>[10]</sup> Thus post-deposition curing to increase the network connectivity by formation of Si-O-Si bonds has been critical to achieve acceptable mechanical properties at the expense of organic component loss, film shrinkage, and degradation of electro-optical performance that accompanies curing.<sup>[11–13]</sup> The effect of network connectivity on mechanical

[\*] M.S. Oliver, Dr. G. Dubois, Dr. D. M. Gage, Prof. R. H. Dauskardt  
Department of Materials Science and Engineering  
Stanford University  
Stanford, CA 94305 (USA)  
E-mail: gdubois@us.ibm.com; dauskardt@stanford.edu  
Dr. G. Dubois, Dr. M. Sherwood  
Department of Advanced Organic Materials  
IBM Almaden Research Center  
650 Harry Road, San Jose, CA 95120 (USA)

DOI: 10.1002/adfm.201000558

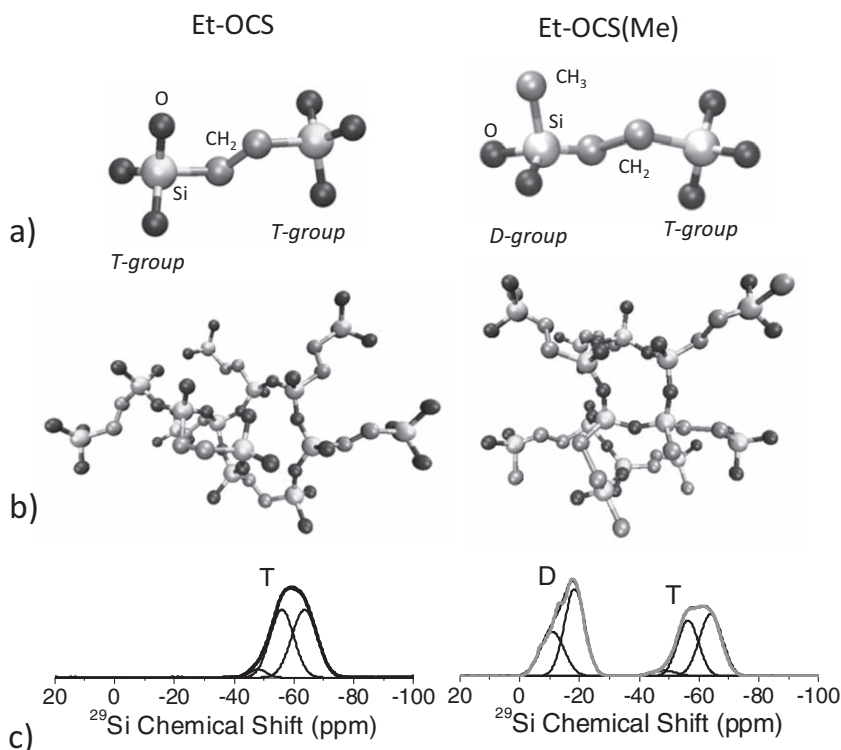


**Figure 1.** Molecular structure of Et-OCS and Et-OCS(Me) organosilicate glasses showing a) the basic structural units and b) clusters of seven basic units. The full simulations contained 750 units in a cubic simulation cell with periodic boundary conditions. Experimental  $^{29}\text{Si}$  NMR spectra of synthesized Et-OCS and Et-OCS(Me) glasses showing the characteristic di-functional (D) and tri-functional (T) peaks are presented in c). The component peaks for the  $D_1$ ,  $D_2$ ,  $T_1$ ,  $T_2$ , and  $T_3$  groups used to calculate the condensation degrees are shown as well.

properties was systematically studied by varying the Si-O-Si condensation degree of the model networks. In addition, by comparing the Et-OCS and Et-OCS(Me) glasses, the impact of the terminal methyl group of the Et-OCS(Me) glass was explored. Experimental characterization of the structure and mechanical properties of synthesized Et-OCS and Et-OCS(Me) glasses was used to both calibrate our models and validate their predictions.

## 2. Results and Discussion

### 2.1. Hybrid Glass Network Connectivity

To precisely quantify network connectivity, we use two metrics. The condensation degree,  $q$ , is equal to the fraction of possible Si-O-Si bonds that have formed and has a maximum value of one regardless of precursor structure. While widely used, condensation degree ignores the influence of bridging and terminal carbon groups on the connectivity of the network. Thus we define the Si-X-Si connectivity,  $p$ , (where X = O or C-C) to equal the fraction of bridging Si-X-Si bonds per silicon atom that are present compared to fully connected  $\text{SiO}_2$ . This metric provides an absolute measure of network connectivity. The maximum possible values of  $p$  for Et-OCS and Et-OCS(Me) are 1.0 and 0.875, respectively. The condensation degree,  $q$ , and Si-X-Si connectivity,  $p$ , are uniquely related for Et-OCS by:

$$p_{\text{Et-OCS}} = (1 + 3q_{\text{Et-OCS}})/4 \quad (1)$$

and for Et-OCS(Me) by:

$$p_{\text{Et-OCS(Me)}} = (1 + 2.5q_{\text{Et-OCS(Me)}})/4 \quad (2)$$

In the following discussion, both metrics will be employed to provide important insights about the relationship between network connectivity and mechanical properties.

To make valid comparison between the model predictions and experimental measurements of mechanical properties, the condensation degrees of the models had to match those of the real glasses. Thus the condensation degree of the synthesized Et-OCS and Et-OCS(Me) glasses were measured using  $^{29}\text{Si}$  NMR spectroscopy. The  $^{29}\text{Si}$  NMR spectra of both the Et-OCS and Et-OCS(Me) glasses are shown in Figure 1c. The characteristic tri-functional (T) and di-functional (D) peaks are apparent. These peaks are composed of  $T_1$ ,  $T_2$ , and  $T_3$  peaks and  $D_1$  and  $D_2$  peaks, respectively, where the subscript denotes the number of bridging Si-O-Si bonds attached to the group. By decomposing the NMR spectra into these components, the network connectivity was determined. The measured values of condensation degree,  $q$ , for the synthesized Et-OCS and Et-OCS(Me) films were 0.818 and 0.820, respectively. These correspond to Si-X-Si connectivity values of 0.864 and 0.763, respectively.

### 2.2. Bulk Modulus

The bulk moduli of the model glasses were simulated by applying hydrostatic pressure in incremental steps and measuring the equilibrated volumetric strain. The bulk moduli of the model glasses are plotted against condensation degree,  $q$ , in Figure 2a along with the experimentally measured values for the real glasses and the bulk modulus of fused  $\text{SiO}_2$  for comparison. At an equivalent condensation degree, the modulus of Et-OCS(Me) was much less than Et-OCS over the entire range of  $q$  values considered. For the real glasses, the bulk modulus values predicted by the model were 13.2 and 6.1 GPa for Et-OCS and Et-OCS(Me), respectively. These values are in excellent agreement with the experimentally measured values of 13.0 and 5.0 GPa. The same data are plotted against Si-X-Si connectivity,  $p$ , in Figure 2b. The data for both glasses follows a similar trend. This indicates that the decrease in elastic stiffness of Et-OCS(Me) can be explained by the reduction in the Si-X-Si connectivity that results from the terminal Si- $\text{CH}_3$  groups. Note that for a given Si-X-Si connectivity, both Et-OCS and Et-OCS(Me) contain the same number of terminal groups but for Et-OCS(Me), some of these groups are Si- $\text{CH}_3$  groups instead of Si-OH or Si-OEt. The composition of the terminal group should have little effect on elastic properties unless it sterically affects the molecular network configuration.

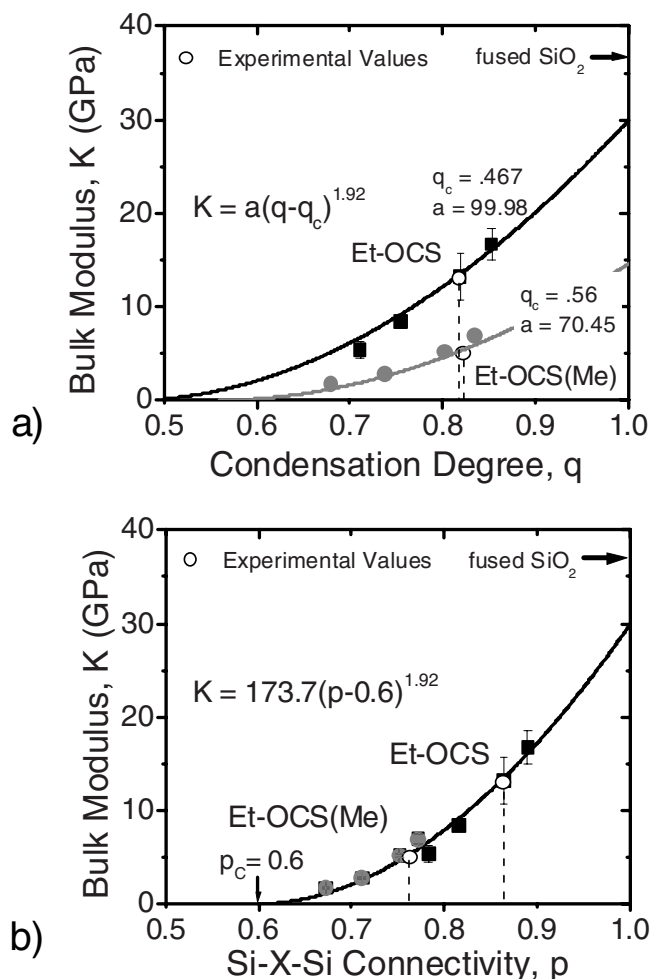


**Figure 2.** Model predictions and experimental measurements of bulk modulus plotted against a) condensation degree,  $q$ , and b) Si-X-Si connectivity,  $p$ . The solid lines are power-law fits to the model data passing through zero at  $p = 0.6$ , the critical Si-X-Si connectivity corresponding the point of rigidity percolation.

To fit the observed scaling of modulus with connectivity, a mean-field model for elastic stiffness was used.<sup>[14]</sup> This model assumes non-linear scaling of modulus with connectivity and zero modulus below the percolation of rigidity, which occurs at a mean coordination of 2.4.<sup>[15]</sup> Modeling the glasses as a network of Si atoms, a mean coordination of 2.4 is equivalent to a Si-X-Si connectivity,  $p$ , of 0.6. At connectivity values below this threshold, the rigid regions of the network do not percolate. Thus we fit the modulus data assuming it scales as  $(p - 0.6)^m$ . A power-law exponent,  $m$ , of 1.92 was found to fit all the data well. In Figure 2a, the data for Et-OCS and Et-OCS(Me) was fit by calculating the critical condensation degrees corresponding to  $p = 0.6$ . From equations 1 and 2, the critical condensation degrees are 0.467 for Et-OCS and 0.56 for Et-OCS(Me). Extrapolation of the fit in Figure 2b predicts a bulk modulus value of 29.9 GPa at  $p = 1.0$ . For comparison the experimentally measured bulk modulus of fused SiO<sub>2</sub> ( $p \approx 1.0$ ) glass is 36.9 GPa. The prediction that a fully connected network with an ethane bridge would have a lower stiffness than silica is reasonable

as the ethane bridge reduces the silica network density. The predicted elastic behavior of the hybrid glasses as a function of the network connectivity is therefore accurately revealed by the simulations and shown to be in excellent agreement with experimentally measured values and well described by a mean-field model of glass network stiffness. These results also demonstrate the importance of accounting for network connectivity when predicting the elastic properties of hybrid glasses. Models that assume full network condensation will be inaccurate.

### 2.3. Cohesive Fracture

Compared to elastic behavior, quantitative prediction of fracture energy is much more challenging as it involves energy dissipation from many possible mechanisms that range from atomistic bond rupture to macroscopic crack tip plasticity. Broadly speaking, the fracture energy expressed as a critical value of the strain energy release rate,  $G_c$  [ $J m^{-2}$ ], can be considered to be the sum of the work of cohesion,  $G_c$ , and the work related to plastic deformation at the crack tip,  $G_{pl}$ . The work of cohesion is related to the energy required to rupture bonds along the fracture path. Micromechanical analysis of brittle fracture has shown that plastic energy dissipation only becomes significant when the material yield strength is less than half the cohesive bond rupture strength.<sup>[16]</sup> For brittle materials such as silica and hybrid glasses, the yield strength at room temperature is approximately equal to the cohesive strength because mechanisms of plastic flow are essentially absent. Thus for the present analysis,  $G_{pl} \approx 0$  and the fracture energy,  $G_c \approx G_0$ . If we further assume that bond rupture is the only contribution then  $G_0$  is simply the product of the density of bonds broken during fracture and the total energy (reversible and irreversible) required to rupture each bond:

$$G_c \approx G_0 = \sum_i \left[ N_i \left( \frac{\text{Bonds}}{\text{Area}} \right) \times (\xi_i + \Delta H_i) \left( \frac{\text{Energy}}{\text{Bond}} \right) \right] \quad (3)$$

where the index  $i$  represents the different bond types,  $N$  is the fracture bond density,  $\Delta H$  is the enthalpy of dissociation, and the factor  $\xi$  is the irreversible energy loss of the bond rupture process. The product of the fracture bond density,  $N$ , and the enthalpy of dissociation,  $\Delta H$ , is the thermodynamic work of fracture. Even for highly brittle solids, the thermodynamic work of fracture is known to underestimate of the fracture energy as other irreversible energy loss mechanisms at the atomic scale are active.<sup>[17]</sup> The factor  $\xi$  can have values on the order of several times  $\Delta H$  due to toughening mechanisms such as bond trapping<sup>[18]</sup> or lattice trapping<sup>[19]</sup> and molecular bridging.<sup>[6,20]</sup>

An accurate estimate of fracture bond density,  $N$ , is very difficult to obtain for hybrid glasses as they have a complex network topology. Additionally, the crack follows a three-dimensional path through the glass network to avoid regions of high bond density.<sup>[11,21]</sup> Existing models of fracture surface bond density,  $N$ , are unable to capture this behavior. The simplest and most often used approximation of  $N$  is to take the two-thirds-root of the volume density of bridging Si-X-Si bonds which provides a mean bond area density. This is referred to here as

the *volume* model. While providing an order-of-magnitude estimate, this model does not account for bond orientation or out-of-plane oscillations of the fracture surface. A better method is to compute the number of Si-X-Si bonds intersected by a two-dimensional plane passing through a model network. This is referred to here as the *planar-cut* model. This method accounts explicitly for bond orientation and network topology but still does not allow for fracture path oscillations in the out-of-plane dimension.

To properly capture the nature of the fracture path at the atomic-scale we need to compute the three-dimensional path through the molecular network that breaks the fewest number of atomic bonds. We would also like to account for the effect of bond strength on crack path selection. For a complex molecular network this calculation can be accomplished with the application of graph theory. Our fracture model involves converting the model glass networks generated with molecular dynamics into a graph by treating every atom as a node and every bond as an edge. Computing the fracture path is then mathematically equivalent to finding the *minimum-cut* (min-cut) of the graph. The “capacity” of the cut is related to the capacity of the edges which can be related to reported values of the Si-O, Si-C and C-C bond strengths.<sup>[22]</sup> The min-cut algorithm numerically finds a set of bonds that has the minimum number of bonds and that completely separates the network if removed. Thus the type and position of all bonds ruptured as well as the three-dimensional fracture path topography can be predicted.

An important consideration is that the model is rooted in the Griffith description of fracture and does not explicitly account for crack-tip deformation effects on the fracture path. For brittle amorphous materials, which lack crack tip plasticity, the crack tip deformation can be assumed to be entirely elastic. The fracture path determined by the min-cut algorithm is not affected by even large scale elastic crack-tip deformation as the topology of the network only changes when bonds are broken or rearranged. This important point means that the min-cut fracture path predicted through a molecular network is not sensitive to elastic deformation of the network – the same path including bond density and type would always be activated. Additionally, the ruptured bonds predicted by min-cut are those that are most critical to the load-transfer path through the network and thus will likely experience the highest force and be most likely to break.

To illustrate the behavior of the min-cut fracture model, the dependence of the fracture bond density,  $N$ , on the min-cut height,  $\Delta$ , is shown for a representative Et-OCS model ( $p = 0.842$ ) in Figure 3a. As the min-cut height increased from 0 (the *planar-cut* model) and the fracture path was allowed more freedom in the out-of-plane dimension, the model could find a lower bond density path through the network and thus the fracture bond density decreased. Also shown in Figure 3a is the fracture height,  $h$ , which is the difference in the position between the highest and lowest atoms that are attached to ruptured bonds. When the min-cut height was below about 1 nm, the fracture height equaled the min-cut height, showing that the fracture path was constrained in the out-of-plane dimension. Once the min-cut height was sufficiently large, the fracture height equilibrated at a value of about 1.5 nm. The predicted fracture path is well equilibrated for a min-cut height of

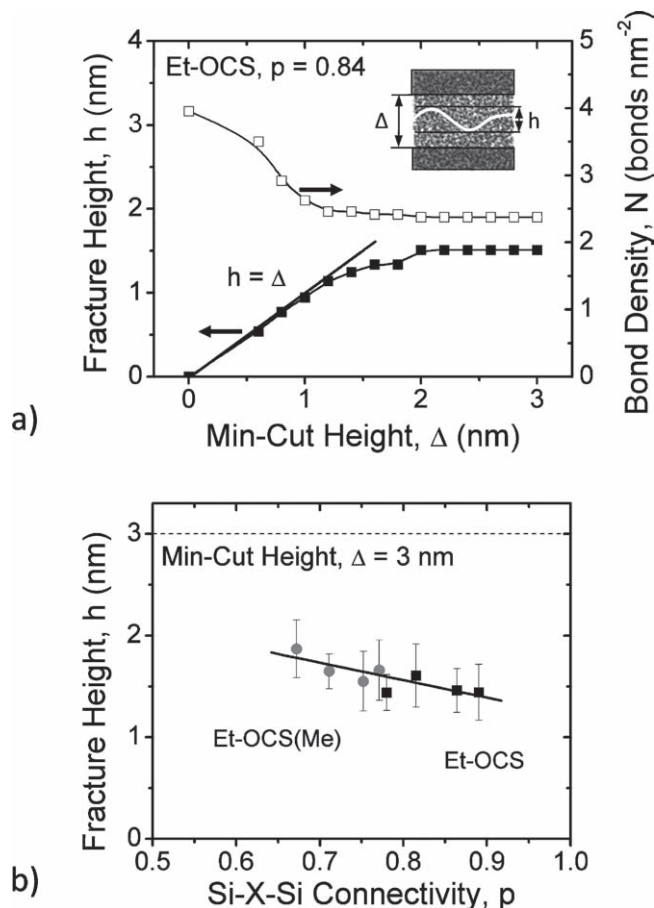


**Figure 3.** Fracture bond density,  $N$ , and fracture height,  $h$ , are shown in a) as a function of min-cut height,  $\Delta$ . The fracture surface height,  $h$ , is plotted as a function of Si-X-Si connectivity,  $p$ , for a min-cut height of 3 nm in b). Error bars represent one standard deviation.

3 nm, and thus the *min-cut* fracture model refers to the fracture path predicted for a min-cut height of 3 nm.

This inherent fracture path oscillation predicted by the model decreased with increasing Si-X-Si connectivity. The fracture height,  $h$ , for both Et-OCS and Et-OCS(Me) is shown as a function of Si-X-Si connectivity in Figure 3b for a min-cut height of 3 nm. The average fracture height values varied from 1.87 nm to 1.44 nm over the Si-X-Si connectivity range considered. The decrease in fracture height with increased connectivity occurred because a deflection of the crack path out of the average plane can either reduce the fracture surface bond density by avoiding a network forming bond or increase the fracture surface bond density by passing through an additional network forming bond. The probability that a deflection of the fracture path intercepts an additional bond increases with network connectivity thus causing the fracture path to remain more planar. The data extrapolates to 1.23 nm at  $p = 1.0$ . For comparison, the peak-to-valley roughness of dense SiO<sub>2</sub> ( $p \approx 1$ ) fracture surfaces has been measured with AFM in ultra-high vacuum to be  $\sim 0.6$  nm over a 2.5 nm  $\times$  2.5 nm area.<sup>[23,24]</sup> Considering the structural differences between Et-OCS and SiO<sub>2</sub> and that the peak-to-valley

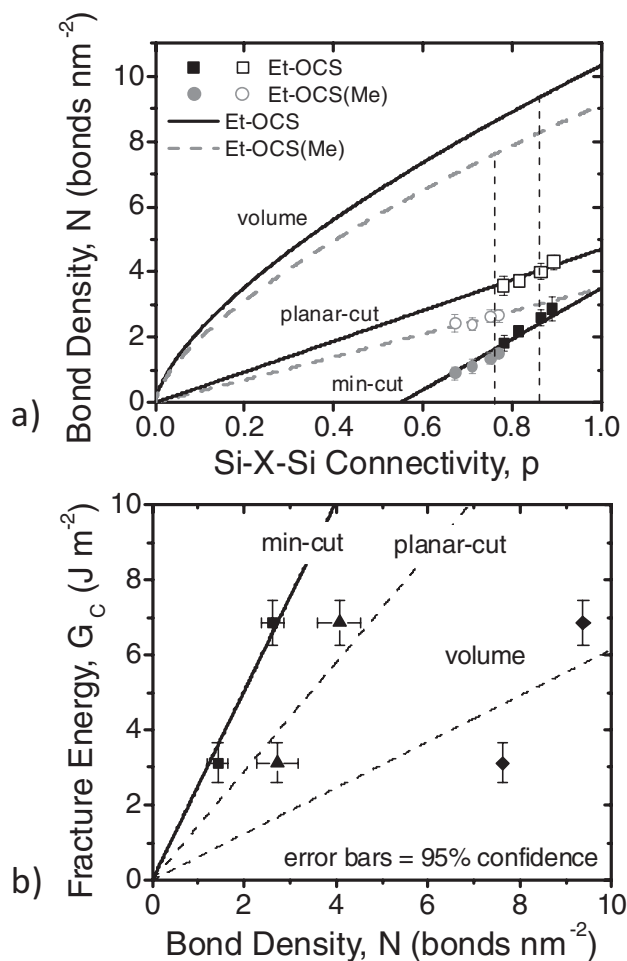


**Figure 4.** a) The fracture surface bond densities of the model networks plotted against Si-X-Si connectivity,  $p$ , predicted by the volume, planar-cut, and min-cut models. The vertical dotted lines mark the values of  $p$  for the real glasses. In b) the experimentally measured fracture energies of Et-OCS and Et-OCS(Me) plotted against the fracture bond densities predicted by the min-cut, planar-cut, and volume models. The fracture energy is proportional to the fracture bond densities predicted by the min-cut model, but not the planar-cut or volume models.

roughness measured by AFM will be several Å less than the fracture height,  $h$ , because of post-fracture surface relaxation and AFM tip shape effects, these values are quite consistent.

In order to predict the influence of network connectivity on  $G_c$ , the influence of connectivity on the fracture bond density,  $N$ , must be understood. The effect of network connectivity on the fracture bond densities for Et-OCS and Et-OCS(Me) is shown in Figure 4a as predicted by the min-cut, planar-cut, and volume models. Compared to the min-cut model, the planar-cut and volume models both predict much higher fracture surface bond densities. Another important difference between the three models is that only the min-cut model predicts the existence of a percolation threshold, below which the glass is disconnected and thus would have approximately zero fracture energy. Such a threshold must exist but is not predicted by either the volume or planar-cut models. Note also that min-cut data for Et-OCS and Et-OCS(Me) fall along a similar trend (as with the bulk

**Table 1.** Fracture bond densities (bonds  $\text{nm}^{-2}$ ) for Et-OCS and Et-OCS(Me) predicted by the min-cut, planar-cut, and volume models.

Model	Et-OCS			Et-OCS(Me)		
	Si-O-Si	Si-C <sub>2</sub> -Si	Total	Si-O-Si	Si-C <sub>2</sub> -Si	Total
Min-Cut	1.29	1.32	2.61	0.53	0.89	1.42
Planar-Cut	2.70	1.33	4.03	1.54	1.12	2.66
Volume	6.30	5.50	9.37	4.84	4.76	7.63

modulus results in Figure 2b) and can be well described by a single linear fit that passes through zero at  $p = 0.55$ . Thus the min-cut model predicts that the fracture bond density,  $N$ , is proportional to  $(p - 0.55)$ . The values of  $p$  for the real Et-OCS and Et-OCS(Me) glasses are highlighted with dotted lines. The total fracture bond densities predicted by the three models for both Et-OCS and Et-OCS(Me) are listed in Table 1 along with the number of Si-O-Si and Si-C-C-Si bonds ruptured.

If the min-cut fracture model is accurate, then fracture energy should be directly proportional to the fracture bond density,  $N$ , predicted by the min-cut model (Equation 3). The experimentally measured fracture energies of Et-OCS and Et-OCS(Me) are plotted against the fracture surface bond densities predicted by the min-cut, planar-cut, and volume fracture models in Figure 4b. The lines represent the best proportional scaling between fracture bond density and  $G_c$ . The planar-cut and volume models clearly do not agree with the measured data. On the other hand, the measured fracture data is most consistent with the min-cut model which reveals the highly proportional relationship between the min-cut bond density and fracture energy values. The value of  $\xi + \Delta H$  predicted by the min-cut model for Et-OCS and Et-OCS(Me) is  $1520 \text{ kJ mol}^{-1}$ . For comparison the enthalpies of dissociation,  $\Delta H$ , for Si-O and Si-C are both roughly  $400 \text{ kJ mol}^{-1}$ , implying the total bond rupture energies are 3 to 4 times  $\Delta H$ . This apparent discrepancy is actually consistent with brittle fracture theory as other energy dissipation mechanisms are active as previously noted.

In the present materials, both bond trapping and molecular bridging mechanisms are expected to contribute significantly to the bond rupture energies. The rupture of Si-O and Si-C bonds in the present materials requires that all bonds in the Si-O-Si and Si-C-C-Si chains, respectively, be loaded to the bond rupture force. Therefore the total work required to rupture the Si-O and Si-C bonds increases. This mechanism is referred to as molecular bridging.<sup>[20]</sup> In addition, to load a Si-X-Si chain to its rupture force, material surrounding the chain must also be loaded. When the bond ruptures, some of the stored elastic energy in the surrounding material is lost as phonons. This mechanism is known as bond trapping.<sup>[18]</sup> Bond trapping is predicted to be most effective for materials with an open network structure and directional chemical bonds which are both characteristics of hybrid glasses.

Knowing now that the fracture energy is proportional to the min-cut bond density (Figure 4b) and that the min-cut bond density is proportional to  $(p - 0.55)$  (Figure 4a), we predict that the fracture energy,  $G_c$ , should follow the same proportionality:

$$G_c \propto N_{\text{min-cut}} \propto (p - 0.55) \quad (4)$$

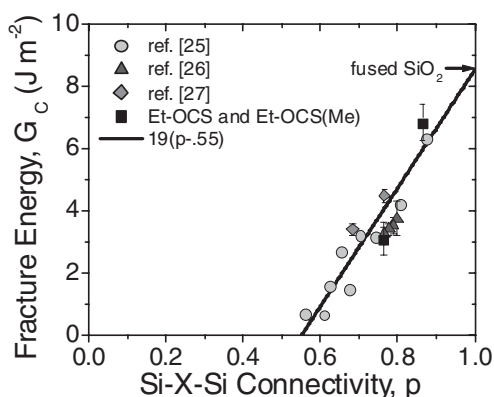


**Figure 5.** Experimentally measured fracture energies of various hybrid glasses are plotted against the Si-X-Si connectivity,  $p$ . Both the fracture bond density,  $N$ , and fracture energy,  $G_c$ , are proportional to  $(p-0.55)$ , demonstrating that fracture energy scales with the min-cut bond density.

The accuracy of this prediction is supported by experimental measurements of fracture energies shown in **Figure 5** for various spin-on and CVD hybrid glasses. Along with data for Et-OCS and Et-OCS(Me), data is shown for spin-on glasses that were processed with various concentrations of terminal Si-CH<sub>3</sub> and Si-H groups.<sup>[25]</sup> The incorporation of terminal groups into the glass decreases the Si-X-Si connectivity (but not necessarily the condensation degree). The condensation degree of these glasses was assumed to be 0.8. Also shown in **Figure 5** is fracture energy data for PECVD hybrid glasses.<sup>[26]</sup> Using the reported ratios of terminal to network bonds, we have calculated the corresponding Si-X-Si connectivity values. Data for other PECVD glasses are also plotted.<sup>[27]</sup> The Si-X-Si connectivity was calculated from the reported mean coordination numbers. The solid line in **Figure 5** shows the fracture energy scaling predicted by the min-cut model assuming a fracture energy of 8.5 J m<sup>-2</sup> at  $p = 1.0$ , which is the fracture energy of dense SiO<sub>2</sub> glass.<sup>[28]</sup> All the data falls along a similar trend and is well fit by the min-cut model. This strongly suggests that fracture energy in hybrid glasses is proportional to the quantity  $(p - 0.55)$  and thus proportional to the min-cut of the glass network.

The scaling of fracture energy with  $(p - 0.55)$  is not simply an empirical relationship but reveals something more fundamental about the connection between fracture energy and network connectivity. The effective medium approximation (EMA) for bond percolation predicts that for a network of  $z$ -coordinated nodes such the  $(1 - p)$  bonds are removed in a perfectly random manner, the minimum-cut of the network is predicted to scale linearly with  $p$  such that the line passes through zero at  $p = 2/z$ .<sup>[29]</sup> Hybrid glasses can be modeled as a network of 4 coordinated Si atoms connected by oxygen or organic bridges and so using the EMA, we can predict that the min-cut bond density and also the fracture energy of hybrid glasses should be proportional to  $(p - 0.50)$ , very similar to the  $(p - 0.55)$  scaling predicting by the min-cut analysis of the molecular glass models. The discrepancy arises from secondary effects related to the specifics of the hybrid glass network structure. For example, while the EMA provides an exact solution for a

two-dimensional square lattice, the EMA provides only an approximation for similar networks. The square, (3,4,6,4), and (3,6,3,6) two-dimensional Archimedean lattices all have a coordination number of four but the bond percolation thresholds of these lattices are 0.5000, 0.5248,<sup>[30]</sup> and 0.5244,<sup>[31]</sup> respectively.

The accuracy of the EMA in predicting the min-cut and fracture energy scaling for hybrid glasses means that remarkably, the fracture energy scaling with connectivity for amorphous, three-dimensional hybrid glasses can be well predicted to first order by modeling the glass network as a square lattice of Si atoms. This result reveals the deep and fundamental connection between fracture energy in brittle glasses and the mathematics of bond percolation theory, providing a simple mathematical framework for understanding and predicting the influence of network connectivity on fracture energy in hybrid glasses and other brittle solids.

### 3. Conclusions

Using a combined computational and synthetic approach, we have established fundamental scaling laws for the elastic and fracture properties of hybrid glasses. A simple mean-field model based on rigidity percolation occurring at Si-X-Si connectivity,  $p$ , of 0.6 could capture the scaling of bulk modulus with connectivity. For the ethane-bridged glasses investigated, the bulk modulus scaled as  $(p - 0.6)^{1.92}$ . The fracture energy of brittle hybrid glasses was shown to scale with  $(p - 0.55)$ , the same scaling as the number of bonds broken during fracture. This remarkably simple relation is rooted in the mathematics of bond percolation theory. These results show that Si-X-Si connectivity,  $p$ , provides the best measure of network connectivity because it provides an absolute measure that is independent of precursor structure. More importantly, it enables application of the powerful results of percolation theory.

We can now explain the paradoxical relative ineffectiveness of some curing strategies at improving cohesive fracture energy in glasses as opposed to their effects on elastic stiffness and adhesive fracture.<sup>[11,12]</sup> While elastic properties are highly sensitive to changes in connectivity induced during curing, the cohesive crack can meander through the network on a path that cleaves the least number of bonds. This additional geometrical freedom results in the insensitivity to cure.

The scaling laws presented will be very useful for the design and optimization of advanced hybrid glasses. While terminal groups are detrimental to mechanical properties, these groups may be beneficial for other properties. An excellent case in point is the field of low dielectric constant (low- $k$ ) materials for microelectronics.<sup>[32]</sup> The majority of low- $k$  materials which are currently incorporated into high performance microprocessors are based on the presence of Si-CH<sub>3</sub> groups in the hybrid material network which provide significant benefits such as etch resistance and hydrophobicity. Understanding the fundamental scaling of stiffness and fracture energy with connectivity (and thus terminal group concentration) will enable optimization of mechanical properties against other property requirements for low- $k$  glasses and also other advanced hybrids whose functionality requires pendent organic groups on the silicon atom.

## 4. Methods

### 4.1. Modeling

**Interatomic Potential:** A number of interatomic potentials for molecular dynamics simulations have been developed to study sol-gel silicate materials and organosilicate molecules.<sup>[33–37]</sup> However none are able to efficiently assemble highly-connected, dense organosilicate networks with controlled network connectivity. We adopt a similar approach to that used to generate model silica glasses with a three-body potential.<sup>[38]</sup> The fundamental structural units for the Et-OCS and Et-OCS(Me) models were Si-(CH<sub>2</sub>)-(CH<sub>2</sub>)-Si and Si-(CH<sub>2</sub>)-(CH<sub>2</sub>)-Si-(CH<sub>3</sub>) bonded molecules, respectively, and oxygen atoms. Hydrogen atoms were modeled implicitly using a united atom approach. Bonds and angles within the Si-C-C-Si and Si-C-C-Si-C chains were modeled as harmonic oscillators. The Si-C-C-Si and C-C-Si-C dihedral angles were modeled with the OPLS dihedral function.<sup>[39]</sup> To create Si-O bonds during the simulation, an empirical potential of the Stillinger-Weber form<sup>[40]</sup> was developed as it allowed for easy control of the Si-O bond length with the two-body term,  $\phi_2(r)$ , and the O-Si-O, Si-O-Si, and O-Si-C bond angles with the three-body term,  $\phi_3(r,s,\theta)$ . The form of the potential energy,  $U(r,s,\theta)$ , is

$$U(r, s, \theta) = \sum_i \sum_{j>i} \phi_2(r_{ij}) + \sum_i \sum_{j \neq i} \sum_{k>j} \phi_3(r_{ij} s_{ik} \theta_{ijk}) \quad (5)$$

where

$$\phi_2(r) = A\epsilon \left[ \left( \frac{\sigma}{r} \right)^m - \left( \frac{\sigma}{r} \right)^n \right] \exp \left( \frac{\sigma}{r - a\sigma} \right)$$

and

$$\phi_3(r, s, \theta) = \lambda\epsilon [\cos \theta - \cos \theta_0] \exp \left( \frac{\gamma\sigma}{r - a\sigma} \right) \exp \left( \frac{\gamma\sigma}{s - a\sigma} \right)$$

For both the two and three body term,  $\sigma$  equals the intercept of potential energy with the r-axis,  $\epsilon$  is the characteristic energy, and  $a$  sets the cut-off distance with respect to sigma (cut-off distance =  $a\sigma$ ). In the two-body term,  $r$  is interatomic distance,  $A$  controls the energy well depth, and  $m$  and  $n$  are the exponents that govern the shape of the pairwise energy function. In the three-body term,  $r$  and  $s$  are interatomic distances,  $\theta$  is the bond angle,  $\theta_0$  is the equilibrium bond angle,  $\lambda$  controls the magnitude of the energy, and  $\gamma$  controls the coupling between the distance and angle energies. The interaction of all non-bonded atom pairs was described by an exponential repulsion function to ensure that atoms did not overlap.

**Model Connectivity:** To control the connectivity of the model networks, the O:Si ratio of the simulation cell was varied. The interatomic potential was designed such that the minimum energy configuration of the simulation was achieved when all possible Si-O bonds were formed. Thus if the O:Si ratio was greater than the stoichiometric ratio for a fully condensed glass (1.5 for Et-OCS and 1.25 for Et-OCS(Me)), then non-bridging oxygen atoms were present. By definition, the Si-X-Si connectivity,  $p$ , and condensation degree,  $q$ , of the Et-OCS and Et-OCS(Me) glasses are uniquely related to the O:Si ratio of the network:

$$p_{\text{Et-OCS}} = (3.5 - (O : Si)) / 2 \quad (6)$$

$$p_{\text{Et-OCS(Me)}} = (3.0 - (O : Si)) / 2 \quad (7)$$

$$q_{\text{Et-OCS}} = 2 - 4(O : Si) / 6 \quad (8)$$

$$q_{\text{Et-OCS(Me)}} = 2 - 4(O : Si) / 5 \quad (9)$$

**Simulated Annealing:** The simulated annealing was done by running NPT molecular dynamics simulations with LAMMPS.<sup>[41]</sup> To generate the model glasses, 750 Si-C-C-Si or Si-C-C-Si-C molecules and the appropriate number of oxygen atoms were placed randomly into a cubic simulation cell with periodic boundary conditions. Initially, a soft potential was used to push overlapping atoms apart. The annealing schedule involved cooling the simulation cell linearly from a temperature of 12 000 K to 6000 K over 10 000 one-femtosecond timesteps then quenching from 6000 K to 300 K over 50 000 femtosecond timesteps. Since the pressure was controlled and not the volume, networks that were more connected had a higher density and than those that were less connected. The same pressure profile was used for all simulations and was chosen such that the densities of the final pressure-free simulation cells representing the experimental glasses were within 5% of the experimentally measured densities (1.539 g cm<sup>-3</sup> for Et-OCS and 1.286 g cm<sup>-3</sup> for Et-OCS(Me)). The pressure decreased linearly over the course of the simulations. The initial pressure was 9 GPa for all simulations. The final simulation cell dimensions varied from 4.8 to 5.5 nm. The accuracy of the local chemical environment of every atom type was verified by analyzing the radial distribution functions and coordination numbers.

**Bulk Modulus:** Using NPT molecular dynamics simulations, the hydrostatic pressure applied to the simulation cell was incremented in a stepwise manner so that the pressure and cell volume could be averaged over 10 000 timesteps. To obtain the bulk modulus, the average pressure was plotted against the average volumetric strain for several applied pressures and the slope was determined with a least-squares fit.

**Min-Cut Cohesive Fracture Model:** In graph theory, a cut is the partitioning of the nodes (atoms) of a graph (glass) into two disjoint sets (separated bodies). The capacity of the cut is the sum of the capacities of the edges connecting the two sets of nodes. A minimum-cut is a cut which has the least capacity. The minimum-cut principle has been used to study cohesion of model polycrystalline solids and simple lattices.<sup>[42–45]</sup> Model glass networks were transformed into graphs by treating every atom as a node and every bond as a weighted edge. Edges were weighted according to bond rupture force. The best measure of bond rupture forces for the bonds present in these materials indicate that the force required to rupture Si-C and Si-O, and C-C bonds are 2.8 nN, 3.3 nN, and 4.1 nN respectively.<sup>[22]</sup> Given the topology of these networks, the relative capacities of the different bond types in the network will not affect the total number of bonds intersected by the min-cut provided that the capacities are within a factor of two. To ensure that the min-cut separated opposite faces of the simulation cell, the tops and bottoms of each cell were consolidated such that the min-cut surface was confined to a plane of height  $\Delta$ . The push-relabel algorithm was

used to find the minimum-cut of the model networks.<sup>[46]</sup> This was done with the MatlabBGL graph library.<sup>[47]</sup>

## 4.2. Experimental Section

**Materials:** To prepare Et-OCS(Me) solution a 20 mL scintillation glass vial, 1.25 g of 1-(triethoxysilyl)-2-(diethoxymethylsilyl)ethane (TESDMSE) is mixed with 3.75 g of 1-methoxy-2-propanol (PMOH) to prepare a 25 wt. % solution. Finally, 0.625 g of a 1 M solution of aqueous nitric acid is added and the solution is allowed to stand without stirring for 1 h at room temperature. Details of Et-OCS film preparation have been reported previously.<sup>[6]</sup> Thin films (400 to 900 nm) were obtained by spin casting the above solutions on clean silicon wafers. The films were first pre-baked at 85 °C for 2 min, then heated under nitrogen from 25 °C to 425 °C at 5 °C min<sup>-1</sup> and held at 425 °C for 1 h using a YES polyimide bake oven.

**Film Density:** Specular x-ray reflectivity measurements were used to determine samples density and these were performed using a diffractometer (X'Pert Pro MRD, Panalytical) with ceramic X-ray tube (wavelength = 0.154 nm) and high resolution horizontal goniometer (reproducibility +/- 0.0001 degree). The critical angles from the reflectivity data were obtained from the peak position of  $Iq^4$  vs.  $q$  plots ( $q = 4\pi/\lambda$ )sin $\theta$ , where  $\lambda$  is the wavelength,  $\theta$  is the grazing incident angle of the X-ray beam).

**Solid-State NMR:** Cross-polarization (CP) magic-angle-spinning (MAS) <sup>29</sup>Si NMR spectra were obtained using a Bruker Avance 500 spectrometer operating at 99.359 MHz and 500.139 MHz for <sup>29</sup>Si and <sup>1</sup>H, respectively. Spectra were obtained using ramped-amplitude cross polarization<sup>[48]</sup> with a 10 ms contact time and two-pulse phase-modulated (TPPM) <sup>1</sup>H decoupling.<sup>[49]</sup> The amplitude of the <sup>29</sup>Si spin locking field was ramped from 80% to 100% during the contact time and the <sup>1</sup>H decoupling field was 115 kHz ( $\gamma B_1/2IT$ ). The MAS spinning speed was 10 kHz. The sample was scraped from 200 mm silicon wafers, 4 each, using a single edged razor blade. The resulting 57 mg of material was transferred into a 4 mm OD Bruker MAS rotor. The <sup>29</sup>Si chemical shift was externally referenced using a rotor containing liquid tetramethylsilane (TMS). The spectra were obtained by averaging 16 k scans with a recycle delay of 5 s. The condensation degree was obtained by least square fitting of the NMR experimental data. For Et-OCS, three Gaussian peaks with a fixed chemical shift (-63.01, -55.86, -48.62) were used for the fitting. For Et-OCS(Me), five Gaussian peaks with a fixed chemical shift (-63.55, -56.01, -47.96, -18.25, -10.83) were used for the fitting. The peak widths were allowed as a free fitting parameter for both Et-OCS and Et-OCS(Me).

**Mechanical Properties:** Elastic moduli were obtained using surface acoustic wave spectroscopy (SAWS). SAWS studies were performed with a laser-acoustic thin film analyzer (LaWave, Fraunhofer USA) and acoustic waves were generated by a nitrogen pulse laser (wavelength 337 nm, pulse duration 0.5 ns). These were detected using a transducer employing a piezoelectric polymer film as a sensor. The measured surface wave velocity as a function of frequency was fitted with the theoretical dispersion curve to deduce both Young's modulus and bulk modulus (a value of 0.25 was assigned for Poisson's ratio).

Blanket films (400–500 nm) were capped with a 200 nm stiff bilayer of Cr and Al through evaporation. Sandwich fracture testing specimens were fabricated by epoxy bonding the thin-film stacks to blank silicon and then using a high-speed diamond wafering blade to section the bonded wafers into beams of appropriate dimensions. All testing was carried out at 25 °C and ~40% relative humidity using the Delaminator adhesion test system (DTS, Menlo Park, CA). Following mechanical testing, XPS was used to determine the location of failure.

## Acknowledgements

The work was supported by the Director, Office of Energy Research, Office of Basic Energy Sciences, Materials Sciences Division of the U.S.

Department of Energy, under Contract No. DE-FG02-07ER46391. The authors thank Christel Gervais Stary for help with the NMR fit and Willi Volksen for help with thin film preparation.

Received: March 23, 2010

Revised: May 26, 2010

Published online: July 9, 2010

- [1] C. Sanchez, B. Julian, P. Belleville, M. Popall, *J. Mater. Chem.* **2005**, *15*, 3559.
- [2] S. Kirkpatrick, C. D. Gelatt, M. P. Vecchi, *Science* **1983**, *220*, 671.
- [3] N. Tajima, T. Ohno, T. Hamada, K. Yoneda, N. Kobayashi, S. Hasaka, M. Inoue, *Appl. Phys. Lett.* **2006**, *89*, 061907.
- [4] N. Tajima, T. Ohno, T. Hamada, K. Yoneda, S. Kondo, N. Kobayashi, M. Shinriki, Y. Inaishi, K. Miyazawa, K. Sakota, S. Hasaka, M. Inoue, *Jpn. J. Appl. Phys.* **2007**, *46*, 5970.
- [5] H. S. Choi, T. Lee, H. Lee, J. Kim, K. Hong, K. H. Kim, J. Shin, H. J. Shin, H. D. Jung, S. H. Choi, *Mater. Res. Soc. Symp. Proc.* **2006**, *891*.
- [6] G. Dubois, W. Volksen, T. Magbitang, R. D. Miller, D. M. Gage, R. H. Dauskardt, *Adv. Mater.* **2007**, *19*, 3989.
- [7] G. Dubois, W. Volksen, T. Magbitang, M. H. Sherwood, R. D. Miller, D. M. Gage, R. H. Dauskardt, *J. Sol-Gel Sci. Technol.* **2008**, *48*, 187.
- [8] H. W. Ro, K. Char, E. C. Jeon, H. J. Kim, D. Kwon, H. J. Lee, J. K. Lee, H. W. Rhee, C. L. Soles, D. Y. Yoon, *Adv. Mater.* **2007**, *19*, 705.
- [9] J. S. Rathore, L. V. Interrante, G. Dubois, *Adv. Funct. Mater.* **2008**, *18*, 4022.
- [10] E. P. Guyer, M. Patz, R. H. Dauskardt, *J. Mater. Res.* **2006**, *21*, 882.
- [11] D. M. Gage, J. F. Stebbins, L. M. Peng, Z. J. Cui, A. Al-Bayati, K. P. MacWilliams, H. M'Saad, R. H. Dauskardt, *J. Appl. Phys.* **2008**, *104*, 043513.
- [12] T. S. Kim, N. Tsuji, N. Kemeling, K. Matsushita, D. Chumakov, H. Geisler, E. Zschech, R. H. Dauskardt, *J. Appl. Phys.* **2008**, *103*, 064108.
- [13] T. S. Kim, N. Tsuji, K. Matsushita, N. Kobayashi, D. Chumakov, H. Geisler, E. Zschech, R. H. Dauskardt, *J. Appl. Phys.* **2008**, *104*, 071902.
- [14] H. He, M. F. Thorpe, *Phys. Rev. Lett.* **1985**, *54*, 2107.
- [15] G. H. Dohler, R. Dandoloff, H. Bilz, *J. Non-Cryst. Solids* **1980**, *42*, 87.
- [16] V. Tvergaard, J. W. Hutchinson, *J. Mech. Phys. Solids* **1992**, *40*, 1377.
- [17] P. Gumbsch, R. M. Cannon, *MRS Bulletin* **2000**, *25*, 15.
- [18] G. Schoeck, W. Pichl, *Phys. Status Solidi A* **1990**, *118*, 109.
- [19] R. Thomson, C. Hsieh, V. Rana, *J. Appl. Phys.* **1971**, *42*, 3154.
- [20] D. A. Maidenberg, W. Volksen, R. D. Miller, R. H. Dauskardt, *Nature Mater.* **2004**, *3*, 464.
- [21] F. Iacopi, G. Beyer, Y. Travaly, C. Waldfried, D. M. Gage, R. H. Dauskardt, K. Houthoofd, P. Jacobs, P. Adriaensens, K. Schulze, S. E. Schulz, S. List, G. Carlotti, *Acta Materialia* **2007**, *55*, 1407.
- [22] M. Grandbois, M. Beyer, M. Rief, H. Clausen-Schaumann, H. E. Gaub, *Science* **1999**, *283*, 1727.
- [23] J. F. Poggemann, A. Goss, G. Heide, E. Radlein, G. H. Frischat, *J. Non-Cryst. Solids* **2001**, *281*, 221.
- [24] J. F. Poggemann, G. Heide, G. H. Frischat, *J. Non-Cryst. Solids* **2003**, *326*, 15.
- [25] L. Wang, J. Rim, F. Oota, R. H. Dauskardt, *unpublished work, Stanford University*, **2001**.
- [26] Y. Lin, Y. Xiang, T. Y. Tsui, J. J. Vlassak, *Acta Mater* **2008**, *56*, 4932.
- [27] F. Iacopi, G. Beyer, Y. Travaly, C. Waldfried, D. M. Gage, R. H. Dauskardt, K. Houthoofd, P. Jacobs, P. Adriaensens, K. Schulze, S. E. Schulz, S. List, G. Carlotti, *Acta Mater* **2007**, *55*, 1407.

- [28] J. P. Lucas, N. R. Moody, S. L. Robinson, J. Hanrock, R. Q. Hwang, *Scr. Metall. Mater.* **1995**, 32, 743.
- [29] S. Kirkpatrick, *Rev. Mod. Phys.* **1973**, 45, 574.
- [30] R. Parviainen, *J. Phys. A* **2007**, 40, 9253.
- [31] R. M. Ziff, P. N. Suding, *J. Phys. A* **1997**, 30, 5351.
- [32] W. Volksen, R. D. Miller, G. Dubois, *Chem. Rev.* **2010**, 110, 54.
- [33] S. Bhattacharya, J. Kieffer, *J. Chem. Phys.* **2005**, 122.
- [34] N. Z. Rao, L. D. Gelb, *J. Phys. Chem. B* **2004**, 108, 12418.
- [35] J. Sefcik, S. E. Rankin, *J. Phys. Chem. B* **2003**, 107, 52.
- [36] A. Striolo, C. McCabe, P. T. Cummings, *J. Phys. Chem. B* **2005**, 109, 14300.
- [37] A. Striolo, C. McCabe, P. T. Cummings, *J. Chem. Phys.* **2006**, 125, 104904.
- [38] B. P. Feuston, S. H. Garofalini, *J. Chem. Phys.* **1988**, 89, 5818.
- [39] W. L. Jorgensen, D. S. Maxwell, J. TiradoRives, *J. Am. Chem. Soc.* **1996**, 118, 11225.
- [40] F. H. Stillinger, T. A. Weber, *Phys. Rev. B* **1985**, 31, 5262.
- [41] S. Plimpton, *J. Comput. Phys.* **1995**, 117, 1.
- [42] M. J. Alava, P. M. Duxbury, *Phys. Rev. B* **1996**, 54, 14990.
- [43] A. A. Middleton, *Phys. Rev. E* **1995**, 52, R3337.
- [44] A. T. Ogielski, *Phys. Rev. Lett.* **1986**, 57, 1251.
- [45] E. A. Holm, *J Am Ceram Soc* **1998**, 81, 455.
- [46] A. V. Goldberg, R. E. Tarjan, *J. Assoc. Comput. Machin.* **1988**, 35, 921.
- [47] D. F. Gleich, *Models and Algorithms for PageRank Sensitivity*, Ph.D Thesis, Stanford University, **2009**.
- [48] G. Metz, X. Wu, S. O. Smith, *J. Magn. Reson., Ser. A* **1994**, 110, 219.
- [49] A. E. Bennett, C. M. Rienstra, M. Auger, K. V. Lakshmi, R. G. Griffin, *J. Chem. Phys.* **1995**, 103, 6951.